

First-principles investigation of magnetic properties in hyperkagome Mn_3TSi (T = Co, Rh, Ir) lattice

Peng Ren(任鹏), Xiaosheng Ni(倪晓升), Xunwu Hu(胡训武), and Kun Cao(曹坤)
Citation: Chin. Phys. B, 2026, 35 (**5**): 057502. DOI: 10.1088/1674-1056/ae156c
http://cpb.iphy.ac.cn; http://iopscience.iop.org/cpb

What follows is a list of articles you may be interested in

Wideband near-infrared emission from $GaScO_3:Cr^{3+}$ phosphors with a perovskite structure

Chong Li(李翀), Mengyu Zhang(张梦宇), Chuancheng Zhang(张传成), Wenzhi Su(宿文志), Yong Zou(邹勇), Shoujun Ding(丁守军), and Qingli Zhang(张庆礼)
Chin. Phys. B, 2025, 34 (**8**): 087502. DOI: 10.1088/1674-1056/add506

First- and second-order magnonic topologies in the ferromagnetic breathing SSH model modulated by non-Hermitian effects

Huasu Fu(付华宿), Lichuan Zhang(张礼川), Rami Mrad, Yuee Xie(谢月娥), and Yuanping Chen(陈元平)
Chin. Phys. B, 2025, 34 (**6**): 067506. DOI: 10.1088/1674-1056/addaa0

Distance-dependent magnetization modulation induced by inter-superatomic interactions in Cr-doped $Au_6Te_{12}Se_8$ dimers

Yurou Guan(官雨柔), Nanshu Liu(刘南舒), Cong Wang(王聪), Fei Pang(庞斐), Zhihai Cheng(程志海), and Wei Ji(季威)
Chin. Phys. B, 2024, 33 (**12**): 127502. DOI: 10.1088/1674-1056/ad8625

Low-temperature heat transport of the zigzag spin-chain compound $SrEr_2O_4$

Liguo Chu(褚利国), Shuangkui Guang(光双魁), Haidong Zhou(周海东), Hong Zhu(朱弘), and Xuefeng Sun(孙学峰)
Chin. Phys. B, 2022, 31 (**8**): 087505. DOI: 10.1088/1674-1056/ac5e97

Magnetic excitations of diagonally coupled checkerboards

Tingting Yan(颜婷婷), Shangjian Jin(金尚健), Zijian Xiong(熊梓健), Jun Li(李军), and Dao-Xin Yao(姚道新)
Chin. Phys. B, 2021, 30 (**10**): 107505. DOI: 10.1088/1674-1056/ac1b94

First-principles investigation of magnetic properties in hyperkagome Mn_3TSi (T = Co, Rh, Ir) lattice

Peng Ren(任鹏)[1], Xiaosheng Ni(倪晓升)[1,2], Xunwu Hu(胡训武)[3,†], and Kun Cao(曹坤)[1,‡]

[1] *Center for Neutron Science and Technology, Guangdong Provincial Key Laboratory of Magnetoelectric Physics and Devices, State Key Laboratory of Optoelectronic Materials and Technologies, School of Physics, Sun Yat-Sen University, Guangzhou* 510275, *China*
[2] *Peng Cheng Laboratory, Frontier Research Center, Shenzhen* 518055, *China*
[3] *Department of Physics, College of Physics and Optoelectronic Engineering, Jinan University, Guangzhou* 510632, *China*

(Received 25 August 2025; revised manuscript received 16 October 2025; accepted manuscript online 21 October 2025)

Based on first-principles calculations, we systematically investigate the electronic structures and magnetic properties of the hyperkagome lattice Mn_3TSi. The Fermi surface topologies of Mn_3RhSi and Mn_3IrSi exhibit notable similarities to each other but differ significantly from that of Mn_3CoSi. Competing antiferromagnetic interactions stabilize a 120° non-collinear triangular antiferromagnetic order, with spins canting out of the triangle planes, which leads to strong magnetic frustration. Itinerant magnetism, characterized by significant longitudinal spin fluctuations, especially in Mn_3CoSi, is described using the Heisenberg–Landau Hamiltonian, resulting in an approximate 5% suppression of the Néel temperatures. Linear spin-wave theory reveals pronounced magnetic excitations at $Q = 1.7$ Å^{-1} in polycrystalline powder spectra of Mn_3CoSi and Mn_3RhSi, showing excellent agreement with experimental observations. Spin wave excitations for single crystals of all the three compounds are further predicted, with excitation energies reaching up to around 140 meV. Our findings advance the understanding of frustrated magnetism in hyperkagome lattices.

Keywords: hyperkagome lattice, density functional theory, Heisenberg–Landau Hamiltonian, magnetic excitations

PACS: 75.10.–b, 71.15.Mb, 75.25.–j, 75.30.Ds

DOI: 10.1088/1674-1056/ae156c **CSTR:** 32038.14.CPB.ae156c

1. Introduction

The hyperkagome lattice represents a three-dimensional analogue of the well-known kagome lattice,[1–3] which has been extensively studied as a platform for geometrically frustrated spin systems.[4–6] A notable realization of this lattice geometry is found in the β-Mn structure, where magnetic Mn atoms reside at the 12*d* Wyckoff positions, while non-magnetic Mn atoms are located at the 8*c* sites. This unique atomic configuration can give rise to pronounced geometric spin frustration and enhance zero-point quantum spin fluctuations, rendering β-Mn a compelling candidate for a three-dimensional quantum spin liquid.[7,8]

The intermetallic compounds Mn_3TSi (T = Co, Rh, Ir), which crystallize in the β-Mn-type structure, serve as prototypical examples of hyperkagome antiferromagnets.[9–12] In these materials, the magnetic Mn atoms form a three-dimensional network of corner-sharing triangles within a non-centrosymmetric framework, where the non-magnetic Mn sites are occupied by transition metal (Co, Rh, Ir) or Si atoms.[8] All three compounds exhibit non-collinear antiferromagnetic (NC-AFM) ordering with distinct triangular spin motifs.[13–15] The NC-AFM arises from the magnetic frustration involving the first, second, and third nearest-neighbor (NN) Mn spin pairs, which adopt a 120° spin arrangement instead of an antiparallel alignment. Mn_3CoSi exhibits a Néel temperature (T_N) of 140 K, with short-range magnetic correlations persisting up to 240 K.[10] Its magnetic susceptibility deviates from the Curie–Weiss behavior in the paramagnetic phase, signaling the presence of significant magnetic frustration.[10] Mn_3RhSi shows a higher T_N of 190 K with short-range correlations extending up to 720 K.[9,12] Radial spin correlation analysis based on experimental data reveals strong AFM interactions between NN Mn spins and ferromagnetic (FM) correlations between the fifth NN spins, highlighting a highly frustrated magnetic environment.[12,16] Additionally, spiral spin clusters have been observed in the paramagnetic phase of Mn_3RhSi, likely arising from the geometric frustration inherent to the hyperkagome lattice.[12] Among these three compounds, Mn_3IrSi displays the highest T_N of 230 K.[11,13,15] Remarkably, it also exhibits both giant spin Hall and Edelstein effects, despite its weak intrinsic spin–orbit coupling (SOC).[17] Spin dynamics of these materials has also been studied by inelastic neutron-scattering experiments. In Mn_3CoSi, magnetic excitations appear at a momentum transfer of $Q = 1.7$ Å^{-1}, with characteristic energy peaks located around 140 meV,[10] which closely resemble the excitation spectra reported for Mn_3RhSi.[18] These observations

†Corresponding author. E-mail: huxunwu@jnu.edu.cn
‡Corresponding author. E-mail: caok7@mail.sysu.edu.cn

© 2026 Chinese Physical Society and IOP Publishing Ltd. All rights, including for text and data mining, AI training, and similar technologies, are reserved.

underscore the coherent nature of spin excitations across the Mn_3TSi compounds. Given the evident strong magnetic frustration and complex spin dynamics in the Mn_3TSi, a comprehensive theoretical study of their magnetic properties is highly desirable.

In this work, we systematically investigate the electronic structures and magnetic properties of Mn_3TSi compounds using first-principles calculations. The Fermi surface topologies of Mn_3RhSi and Mn_3IrSi exhibit striking similarities but differ significantly from that of Mn_3CoSi. Our calculations reveal that competing AFM interactions stabilize a 120° non-collinear triangular AFM order, with spins canting out of the triangle planes. The resulting strong magnetic frustration originates from the Mn atoms at the vertices of corner-sharing triangles, where it is geometrically forbidden to simultaneously satisfy all three AFM exchange interactions. The itinerant character of the magnetism in Mn_3TSi, manifested through longitudinal spin fluctuations, is incorporated into our modeling via a Heisenberg–Landau Hamiltonian, which is found to result in an approximate 5% suppression of T_N. Linear spin wave theory (LSWT) reveals magnon excitations at $Q = 1.7$ Å^{-1} in polycrystalline powder spectra of Mn_3CoSi and Mn_3RhSi, which are in excellent agreement with experimental data. For Mn_3IrSi, we also predict strong magnon excitation at $Q = 1.7$ Å^{-1}. Spin wave excitations in single crystals of all three compounds are further evaluated, with excitation energies reaching up to around 140 meV. These findings provide a reliable microscopic understanding of the underlying magnetic interactions, encompassing both the exchange parameters and the role of geometric frustration. This framework further captures the subtle interplay between local magnetic moments and itinerant electrons, offering a comprehensive description of the magnetic properties of the Mn_3TSi systems.

2. Computational details

First-principles calculations are performed within the framework of density functional theory (DFT) as implemented in the Vienna *ab initio* simulation package (VASP).[19,20] The projector augmented-wave (PAW) method[21] is employed, with a plane-wave energy cutoff of 500 eV. The exchange–correlation functional is treated using the generalized gradient approximation (GGA) with the Perdew–Burke–Ernzerhof (PBE) formulation.[22] Brillouin zone integrations are performed using a Γ-centred $8 \times 8 \times 8$ Monkhorst–Pack k-point mesh. Experimental lattice constants are adopted[9–11] with atomic positions relaxed until the forces acting on each atom are less than 10^{-3} eV/Å. The total energy convergence criterion for self-consistent calculations is set to 10^{-6} eV. Crystal structures, Fermi surface, and Brillouin zone are visualized using VESTA,[23] IFermi,[24] and VASPKIT,[25] respectively.

The Heisenberg exchange parameters are extracted using the energy mapping method,[26–29] where a $2 \times 2 \times 1$ supercell is employed to construct over 100 distinct magnetic configurations by applying small-angle rotations around the ground-state magnetic configuration. To ensure the applicability of the Heisenberg model, the variation of each local moment is kept below 0.1 μ_B. The Landau expansion coefficients are obtained by fitting constrained magnetic moment calculations (see Appendix B for details).[30–33] The T_N is estimated using replica-exchange Monte Carlo (re-MC) simulations,[34–36] and LSWT calculations are performed with the SpinW package,[37] with the spin quantum number set to $S = 3/2$.

3. Results and discussion

3.1. Crystal structure and magnetic ground state

The Mn_3TSi compounds crystallize in a noncentrosymmetric cubic structure with a space group $P2_13$ (No. 198),[18]

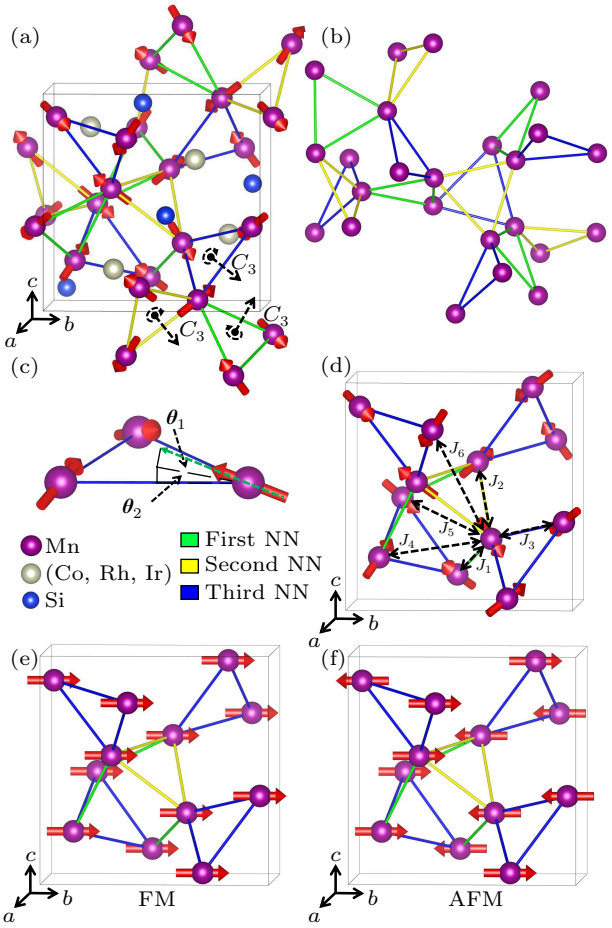


Fig. 1. Crystal and magnetic structures of Mn_3TSi. (a) Purple, light gray, and blue spheres represent Mn, T (Co, Rh, Ir), and Si atoms, respectively. Green, yellow, and blue bonds denote the first-, second-, and third-NN, respectively. Red arrows indicate the magnetic moments of Mn atoms. Black dashed arrows highlight the threefold rotational symmetry (C_3). (b) Hyperkagome lattice structure formed by Mn atoms. (c) Definition of the spin canting angles: θ_1 represents the angle between spin and the corresponding triangular plane. θ_2 denotes the angle between the projection of spin onto the triangular plane and the edge of the triangle. (d) Bonds associated with the considered Heisenberg exchange coupling are marked by black dashed lines. (e) FM configuration and (f) collinear AFM configuration.

as shown in Fig. 1(a). The lattice constants are $a = b = c =$ 6.21 Å for Mn_3CoSi,[10] 6.45 Å for Mn_3RhSi,[9] and 6.49 Å for Mn_3IrSi.[11] Each unit cell contains twelve magnetic Mn atoms occupying the 12*b* Wyckoff sites, which correspond to the 12*d* positions in the parent β-Mn structure. The remaining atomic sites are occupied by four non-magnetic transition-metal atoms (Co, Rh, or Ir) and four Si atoms, which occupy two inequivalent 4*a* Wyckoff sites, resulting from the splitting of the 8*c* sites in the β-Mn prototype.[9–11] This specific atomic arrangement forms a three-dimensional hyperkagome lattice of interconnected Mn triangles (Fig. 1(b)), leading to three types of Mn–Mn bonds within the triangles, with bond lengths ranging from 2.4 Å to 2.8 Å.[38–40] The overall crystal structure, together with the local triangular geometry, preserves a threefold rotational symmetry C_3, with rotation axis along the [111] direction, as demonstrated in Fig. 1(a).

To investigate the magnetic ground state of Mn_3TSi compounds, we perform DFT calculations of total energies for FM, collinear AFM, and the 120° NC-AFM configurations (see Fig. 1). The resulting energies and magnetic moments are summarized in Table 1. For all three compounds, both FM and collinear AFM states have energies higher than the NC-AFM state, indicating that the NC-AFM configuration is the magnetic ground state, in agreement with experimental observations.[9–11] The spins on each triangle exhibit canting out of the corresponding triangle plane, with similar canting angles across different triangles (see Figs. 1(c) and 1(d)). For example, the calculated canting angles for the third NN spins are $\theta_1 = 23.07°$, $\theta_2 = 4.12°$ for Mn_3CoSi; $\theta_1 = 20.60°$, $\theta_2 = 5.62°$ for Mn_3RhSi; and $\theta_1 = 21.13°$, $\theta_2 = 7.35°$ for Mn_3IrSi, in good agreement with experiment.[9–11]

3.2. Electronic structures

The calculated density of states (DOS) for Mn_3TSi in their NC-AFM ground states is shown in Figs. 2(a)–2(c). The DOS shows a finite value at the Fermi level for all three compounds, indicating that they are metallic. Near the Fermi level, the DOS is dominated by contributions from Mn d orbitals, while the d orbitals of the transition-metal atoms (Co, Rh, and Ir) contribute only marginally. Furthermore, contributions from Si p orbitals are negligible in this energy range, suggesting that the Mn d electrons dominate both the metallic and magnetic behavior. In particular, the magnetic ordering is expected to be driven by direct exchange interactions among these localized d electrons, reflecting a dual character that combines localized magnetic moments with itinerant electron behavior. These results are consistent with the previous electronic structure calculations for Mn_3IrSi, as reported in Ref. [15].

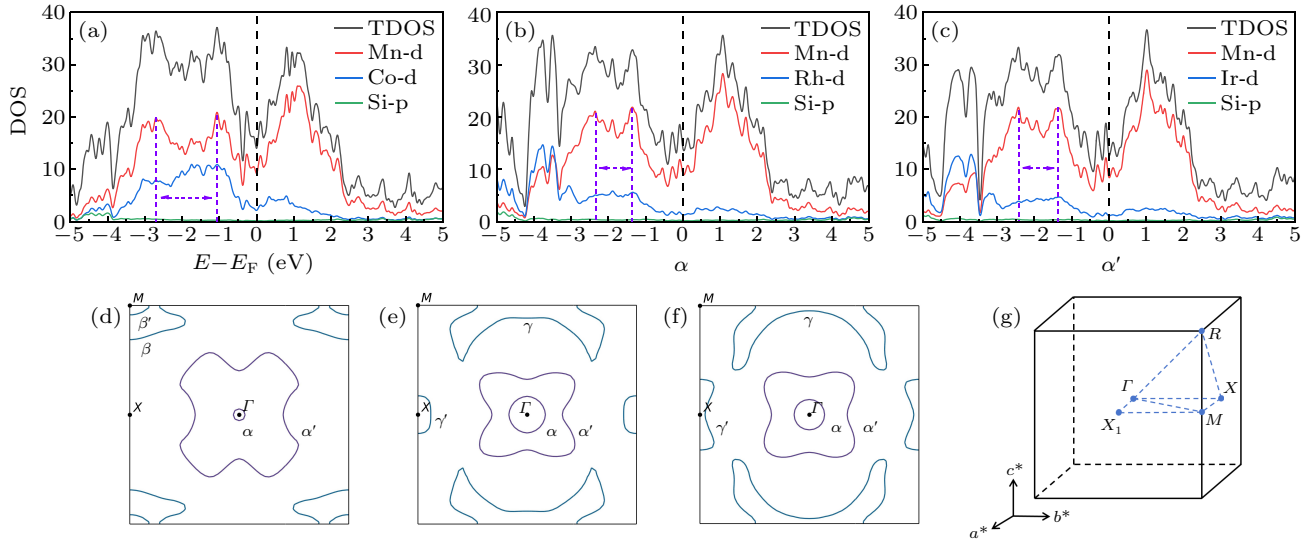


Fig. 2. Electronic structures of Mn_3TSi. The DOS is shown for (a) Mn_3CoSi, (b) Mn_3RhSi, and (c) Mn_3IrSi. Dark grey curves represent the TDOS, while the red, blue, and green lines correspond to the projected DOS of Mn d, Co (Rh, or Ir) d, and Si p orbitals, respectively. The purple dashed lines and arrows indicate the bandwidth of the Mn d orbitals. The Fermi level is indicated by the black dashed line and is set to 0 eV. Panels (d), (e), and (f) show the Fermi surfaces of (d) Mn_3CoSi, (e) Mn_3RhSi, and (f) Mn_3IrSi, respectively, along the Γ–X–M path. (g) The three-dimensional Brillouin zone and its high-symmetry paths follow the sequence Γ–X–M–Γ–R–X|R–M–X_1.

On the other hand, the band structures and DOS reveal a stronger itinerant character in Mn_3CoSi. While Mn_3RhSi (Fig. A1(b)) and Mn_3IrSi (Fig. A1(c)) share similar band dispersions, Mn_3CoSi (Fig. A1(a)) shows notably broader and more dispersive bands near E_F. As shown in Fig. 2(a), the Mn 3d orbitals of Mn_3CoSi dominantly contribute near the Fermi level with relatively large bandwidths. Compared with Mn_3RhSi (Fig. 2(b)) and Mn_3IrSi (Fig. 2(c)), whose Mn 3d states mainly extend from about −2.3 eV to −1.3 eV, the Mn 3d states in Mn_3CoSi span a wider energy range (approximately −2.7 eV to −1.0 eV). This broader bandwidth reflects enhanced electron delocalization and thus a more pro-

nounced itinerant character of Mn_3CoSi. Such itinerancy naturally leads to a broader distribution of local magnetic moments and a stronger sensitivity of $|M|$ to the spin configuration.

The Fermi surfaces of Mn_3TSi compounds are shown in Figs. 2(d)–2(f). For Mn_3CoSi, the Fermi surface consists of two electron pockets (α, β) and two hole pockets (α', β') [see Fig. 2(d)]. In contrast, the Fermi surface of Mn_3RhSi and Mn_3IrSi each contains three electron pockets $(\alpha, \gamma, \gamma')$ and one hole pocket (α'), as shown in Figs. 2(e) and 2(f). Notably, the Fermi surface topologies of Mn_3RhSi and Mn_3IrSi show striking similarities with each other but differ significantly from Mn_3CoSi. In particular, the Fermi surface topology of Mn_3IrSi is consistent with previous findings reported in Ref. [17]. This comparison suggests that Mn_3RhSi and Mn_3IrSi share similar electronic structures and magnetic characteristics, in contrast to those of Mn_3CoSi.

3.3. Magnetic moments

We next examine the magnetic moments of Mn_3TSi compounds in the NC-AFM configuration, with the calculated magnetic moment for each Mn atom $|M|$ shown in Table 1. Although the calculated $|M|$ of Mn_3CoSi (2.55 μ_B) is approximately 42% higher than the experimental value (1.79 μ_B), it is consistent with previous theoretical results.[39] For Mn_3RhSi, the computed $|M|$ is 3.03 μ_B, slightly higher than the experimental value of 2.61 μ_B.[9] In contrast, the calculated $|M|$ of Mn_3IrSi is in close agreement with the experimental value.[11] The calculated $|M|$ in Mn_3CoSi remains over 2.13 μ_B, regardless of whether the local density approximation (LDA) or PBE is used. To further examine the effect of electron correlation, we performed DFT + U calculations with $U_{eff} = 0$–4.0 eV. We found that including U_{eff} further enhances the local Mn moments (up to $\sim$ 3.93 μ_B), thus worsening the comparison with the experiments. Our results suggest that the DFT + U formalism is still incapable of describing the itinerant and frustrated magnetism in Mn_3CoSi.

Table 1. Total energies and Mn magnetic moments for FM, AFM, and NC-AFM (NCM) configurations. The energy of the NC-AFM is set to 0 eV as the reference. Magnetic moments are given in units of the Bohr magneton (μ_B). Exp. denotes experimental values.

	Energy (meV/Mn)			$\|M\|$ (μ_B/Mn)			
	FM	AFM	NCM	FM	AFM	NCM	Exp.
Mn_3CoSi	145.70	45.66	0.00	1.91	2.46	2.55	1.79[10]
Mn_3RhSi	192.47	49.78	0.00	3.04	3.01	3.03	2.61[9]
Mn_3IrSi	196.08	49.04	0.00	3.06	3.01	3.04	2.97[11]

Notably, when the magnetic configuration changes from FM to AFM, the $|M|$ in Mn_3CoSi increases by a substantial 0.55 μ_B, whereas $|M|$ in Mn_3RhSi and Mn_3IrSi remains largely unchanged, suggesting a significantly more itinerant magnetic behavior in Mn_3CoSi. The pronounced reduction of $|M|$ in Mn_3CoSi when the magnetic configuration changes from FM to AFM arises from its stronger character of itinerant magnetism, which, qualitatively, corresponds to a larger band width of magnetic 3d electrons (see Figs. 2(a)–2(c)), leading to stronger hybridization with neighboring magnetic moment (in some cases through ligand ions). Therefore, the change of neighboring magnetic moments, e.g., from FM to AFM, can have a notable impact on the $|M|$.

To further elucidate itinerant behavior, we analyze the total energy dependence on $|M|$, as shown in Fig. 3. The energy minima for Mn_3CoSi, Mn_3RhSi, and Mn_3IrSi are located at 2.55 μ_B, 3.03 μ_B, and 3.04 μ_B, respectively, in good agreement with the corresponding magnetic moments at the ground states. In Mn_3CoSi, the total energy curve exhibits a marked asymmetry around its minimum, with a notably flatter slope on the low-moment side. This shallow energy well is a characteristic feature of strong itinerant magnetism,[30,35] where pronounced longitudinal spin fluctuations can be present in high-energy magnetic states such as the paramagnetic phase. Similar behavior has been reported in prototypical itinerant magnets, such as bcc Fe and fcc Ni.[31–33] In contrast, the energy curves of Mn_3RhSi and Mn_3IrSi exhibit steeper slopes when $|M|$ increases from its ground-state value, and display sharper energy rising when $|M|$ is reduced. The resulting deeper and more symmetric energy wells suggest a tendency toward more localized magnetism, with suppressed longitudinal spin fluctuations.

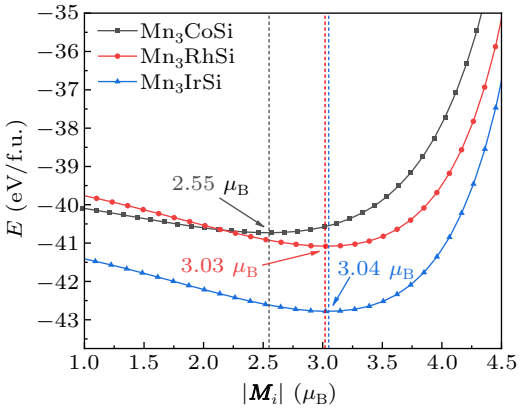


Fig. 3. Variation of Mn magnetic moments as a function of the total energy. Black, red, and blue curves correspond to Mn_3CoSi, Mn_3RhSi, and Mn_3IrSi, respectively. Dashed lines indicate the ground-state magnetic moments for each compound.

We also evaluate the effects of SOC on the Mn magnetic moments. For all three compounds, SOC only has a negligible effect on the total magnetic moments, with the calculated orbital moments all below 0.1 μ_B, indicating strong quenching of the orbital angular momentum due to crystal field effects on the Mn 3d electrons.

3.4. Heisenberg–Landau model

To describe the itinerant magnetism of Mn_3TSi compounds, the Heisenberg–Landau model is employed, which

effectively captures both exchange interactions and longitudinal spin fluctuations.[19,34,35] The corresponding Hamiltonian is given by

$$H = H_{\mathrm{R}} + H_{\mathrm{L}}, \tag{1}$$

$$H_{\mathrm{R}} = \sum_{i<j} J_{ij} \boldsymbol{M}_i \cdot \boldsymbol{M}_j, \tag{2}$$

$$H_{\mathrm{L}} = \sum_i A\boldsymbol{M}_i^2 + \sum_i B\boldsymbol{M}_i^4 + \sum_i C\boldsymbol{M}_i^6 + \sum_i D\boldsymbol{M}_i^8. \tag{3}$$

Here, H_{R} represents the Heisenberg exchange interaction term and H_{L} corresponds to the Landau expansion, capturing energy contributions due to longitudinal spin fluctuations. In this context, $J_{ij} > 0$ indicates AFM interactions, whereas $J_{ij} < 0$ corresponds to FM interactions. Unlike conventional models where $\tilde{J}_{ij}$ is defined for normalized spin directions, here J_{ij} is defined in terms of the full magnetic moments $\boldsymbol{M}_i$, without normalization. Given that the 12 Mn atoms in the unit cell are symmetrically equivalent, a single set of Landau coefficients is used to describe them. The Landau expansion coefficients A, B, C, and D correspond to terms up to the eighth order (see Appendix B for detail). Due to weak SOC in these compounds, magnetocrystalline anisotropy is considered negligible and therefore excluded from the present model.[41]

We focus on the triangular planes formed by the first, second, and third NN Mn atoms. Symmetry analysis reveals that Mn–Mn bonds with identical lengths correspond to equivalent Heisenberg exchange interactions. In total, six inequivalent types of exchange interactions, labeled J_1–J_6, are considered (see Fig. 1(d)). The calculated exchange interactions and Landau expansion parameters are summarized in Tables 2 and 3, respectively. It can be seen that J_1, J_2, and J_3 are dominant AFM interactions, constituting the primary source of magnetic frustration. For spins located at the vertices of the corner-sharing triangles, the AFM J_1–J_3 cannot be simultaneously satisfied due to geometric constraints, leading to the emergence of the NC-AFM ground state.[4] Similar frustration has been observed in kagome lattices, which serve as prototypical examples of frustrated magnetic systems.[41] The longer-range couplings J_4, J_5, and J_6 correspond to interchain interactions, whose strength can be reflected from the ground state spin configurations. Notably, J_5 shows a strong FM interaction, with its magnitude comparable to the average strength of the J_1–J_3, thereby playing a key role in modulating the relative spin directions between different triangles. Similar results have been observed in Co-doped β-Mn, where a fifth-NN FM interaction competes with strong NN AFM interactions.[42] J_4 connects spin pairs of approximately 120°, representing a weak AFM interaction, while J_6 is also a weak interaction connecting spins with relative angles close to 90°. Subsequently, re-MC simulations are performed to investigate the magnetic phase diagrams, with the results summarized in Table 4. Our simulations confirm that the magnetic ground states are all 120° NC-AFM configurations, while the fifth-NN interaction favors FM alignment, consistent with experimental observations.[9–11] Overall, the calculated Heisenberg exchange interactions capture the microscopic origin of magnetic frustration in these compounds.

Table 2. Heisenberg exchange interactions J_{ij} and corresponding bond lengths L for Mn_3CoSi, Mn_3RhSi, and Mn_3IrSi.

	Mn_3CoSi		Mn_3RhSi		Mn_3IrSi	
	J_{ij} (meV)	L (Å)	J_{ij} (meV)	L (Å)	J_{ij} (meV)	L (Å)
J_1	3.52	2.61	2.69	2.69	2.86	2.70
J_2	11.30	2.57	6.59	2.71	6.51	2.71
J_3	4.18	2.65	3.24	2.73	2.63	2.77
J_4	−0.05	3.21	−0.02	3.33	0.41	3.35
J_5	−3.97	3.83	−3.82	3.97	−2.96	3.99
J_6	−0.69	4.27	0.10	4.43	0.23	4.47

Table 3. Landau expansion coefficients for Mn_3CoSi, Mn_3RhSi, and Mn_3IrSi. The coefficients A, B, C, and D are given in units of meV.

	A	B	C	D
Mn_3CoSi	−89.48	10.50	−0.49	0.02
Mn_3RhSi	−156.23	16.43	−0.98	0.04
Mn_3IrSi	−165.18	17.37	−1.04	0.04

Table 4. The T_{N} of Mn_3CoSi, Mn_3RhSi, and Mn_3IrSi in units of K.

	Heisenberg	Heisenberg–Landau	Exp.
Mn_3CoSi	152	148	140[10]
Mn_3RhSi	160	155	190[9]
Mn_3IrSi	150	142	230[11]

Furthermore, when only Heisenberg exchange interactions are considered, the calculated T_{N} for Mn_3CoSi agrees well with experimental results. In contrast, the calculated T_{N} for Mn_3RhSi and Mn_3IrSi are approximately 16% and 35% lower than the corresponding experimental values, respectively. The inclusion of Landau terms further reduces T_{N} by about 5%, highlighting the role of longitudinal spin fluctuations in suppressing T_{N}, which is consistent with previous findings in other itinerant systems, such as $(Fe_{1-x}Ni_x)_5GeTe_2$.[35]

We further investigate the variation of $|\boldsymbol{M}|$ across the phase transitions. The distributions of Mn atoms, obtained from re-MC simulations, are shown in Figs. 4(a)–4(c). In all three compounds, the distribution of $|\boldsymbol{M}|$ is centered around the ground-state values. At $T_{\mathrm{N}} - 40$ K, the distributions are relatively narrow. While at $T_{\mathrm{N}} + 40$ K, they are broaden significantly, reflecting enhanced longitudinal spin fluctuations caused by thermal excitations. Not surprisingly, Mn_3CoSi exhibits the strongest longitudinal spin fluctuations with elevated temperatures, further underscoring its strongly itinerant magnetism. Furthermore, the gradual reduction of the Mn magnetic moment with increasing temperature, as illustrated in Fig. 4(d), further supports the presence of itinerant magnetism.

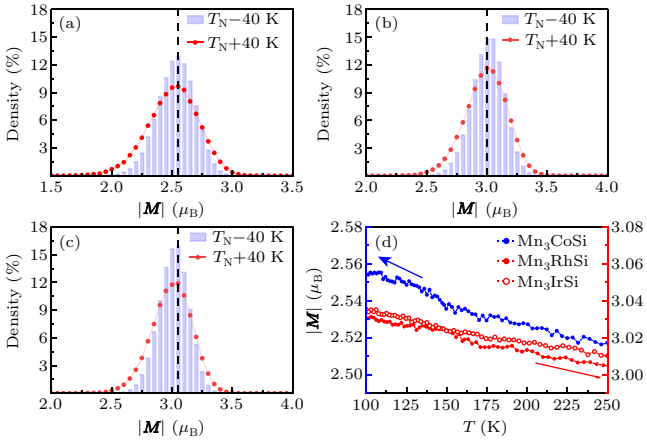


Fig. 4. Local magnetic moment distributions for (a) Mn_3CoSi, (b) Mn_3RhSi, and (c) Mn_3IrSi. Red curves correspond to $T_N + 40$ K, and blue bars to $T_N - 40$ K. Black dashed lines indicate ground-state magnetic moments. (d) Temperature-dependent evolution of magnetic moments for Mn_3CoSi, Mn_3RhSi, and Mn_3IrSi.

Although the itinerancy of Mn_3CoSi is indeed stronger than that in Mn_3RhSi and Mn_3IrSi, the overall degree of itinerancy in all three compounds remains moderate, since all these compounds have a large calculated magnetic moments above 2.50 μ_B. This may explain why the inclusion of longitudinal spin fluctuations leads to a similar reduction of the Néel temperature across these compounds. In systems with more significant itinerant magnetism, such as face-centered cubic (FCC) Ni, which exhibits a ground state magnetic moment of only about 0.7 μ_B, the magnetic moments can be substantially reduced, even to zero, with the increase of temperature above T_c. Inclusion of Landau expansion can significantly reduce the T_c of Fcc Ni. Furthermore, we admit that our model still has certain limitations. In particular, the Heisenberg exchange parameters J_{ij} are assumed to be independent of local magnetic moments, whereas in practice they may vary with moment sizes. The neglect of this dependence could affect the accuracy of the predicted Néel temperatures.

3.5. Magnetic excitations

The spin-wave spectra are calculated by solving the linearized equations of motion based on the DFT calculated Heisenberg exchange interactions, with results shown in Figs. 5(a)–5(c). Twelve distinct magnon branches appear along high-symmetry paths, arising from the breaking of combined spatial-inversion and time-reversal (PT) symmetry, which lifts the Kramers degeneracy. This contrasts with doubly degenerate magnon modes found in conventional collinear AFM systems. Well-defined spin wave dispersions can be found across the sampled paths, with the calculated maximum spin-wave energies of about 138 meV for Mn_3CoSi and 145 meV for Mn_3RhSi, in excellent agreement with the corresponding experimental values of 140 meV.[10,18] For Mn_3IrSi, we predict a maximum excitation energy of 131 meV, which is slightly lower than that of Mn_3CoSi and Mn_3RhSi. However, the LSWT does not take electron–magnon interaction into account. The high energy excitations are expected to experience strong Landau damping due to interaction with spin-flip Stoner excitations.[26,34,43]

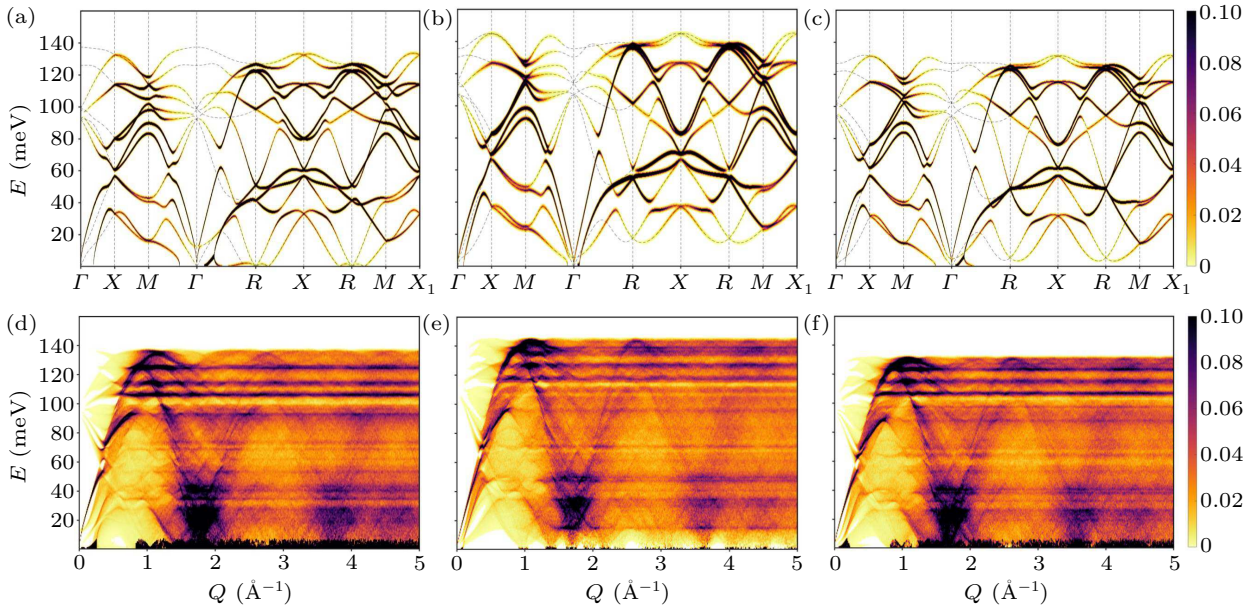


Fig. 5. Calculated spin-wave spectra of (a) Mn_3CoSi, (b) Mn_3RhSi, and (c) Mn_3IrSi. Panels (d)–(f) show the corresponding simulated polycrystalline powder spectra for Mn_3CoSi, Mn_3RhSi, and Mn_3IrSi.

To compare more with experimental results, we also simulate the magnetic excitation spectra of polycrystalline powders, obtained via LSWT with Gaussian convolution (see Figs. 5(d)–5(f)). It can be seen that at low momentum transfer with $Q < 0.5$ Å^{-1}, the excitation energy increases linearly with Q, consistent with classical spin-wave theory for AFM sys-

tems. For Mn_3CoSi and Mn_3RhSi, prominent excitations are observed near 50 meV at $Q = 1.7$ Å^{-1}, which correspond to magnon excitations around the R point (as shown in Figs. 5(a) and 5(b)), in good agreement with experimental data.[12,18] Furthermore, weaker excitations around 40 meV appear at $Q = 3.8$ Å^{-1}. For Mn_3IrSi, we also predict strong magnon excitation at $Q = 1.7$ Å^{-1}. The close agreement between theory and experiment validates the extracted exchange parameters and highlights the effectiveness of the PBE functional in describing magnetic interactions in such hyperkagome materials.

4. Conclusion

In summary, we systematically investigate the electronic structures and magnetic properties of Mn_3TSi compounds using first-principles calculations. The Fermi surface topologies of Mn_3RhSi and Mn_3IrSi exhibit striking similarities, yet differ significantly from that of Mn_3CoSi. Competing AFM interactions, primarily governed by the first, second and third NN exchange interactions, stabilize a 120° non-collinear triangular AFM order, giving rise to strong magnetic frustration. The frustration arises from that the Mn atoms at the vertices of corner-sharing triangles cannot simultaneously satisfy all three AFM interactions. The itinerant nature of magnetism, manifested through pronounced longitudinal spin fluctuations, is incorporated via a Heisenberg–Landau Hamiltonian, leading to an approximate 5% suppression of T_N. LSWT reveals distinct magnetic excitations at $Q = 1.7$ Å^{-1} in Mn_3CoSi and Mn_3RhSi, consistent with experimental data. Spin wave excitations for single crystals of all three compounds are further evaluated, with excitation energies reaching up to around 140 meV. These findings deepen our understanding of magnetic frustration and complex spin dynamics in non-collinear hyperkagome systems.

Appendix A: Band structures

The calculated band structures of Mn_3TSi without SOC are presented in Figs. A1(a)–A1(c). The isostructural cubic compounds share identical three-dimensional Brillouin zones with equivalent high symmetry paths. Notably, several band crossings appear near the Fermi level. Inclusion of SOC induces only minor modifications on the electronic structure. Mn_3CoSi hosts a fourfold degenerate point at the Γ point below the Fermi level, which is not observed in Mn_3RhSi or Mn_3IrSi. All three compounds, however, exhibit multiple degenerate points at the R point. Mn_3RhSi and Mn_3IrSi show strikingly similar band structures near both Γ and R points, contrasting with Mn_3CoSi. Our results are consistent with previous calculations of Mn_3IrSi.[17,44]

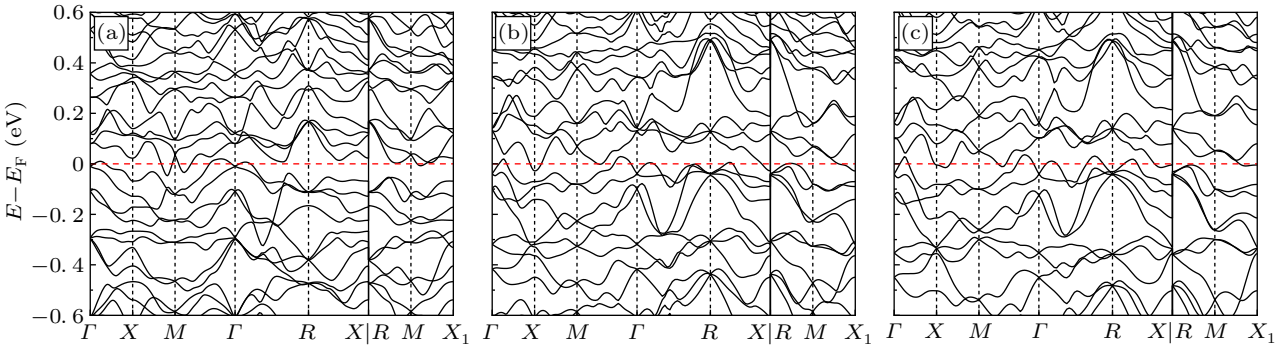


Fig. A1. The band structures are presented for (a) Mn_3CoSi, (b) Mn_3RhSi, and (c) Mn_3IrSi. The red dashed line denotes the Fermi level, set at 0 eV.

Appendix B: Landau expansion

The Landau expansion coefficients are obtained by fitting the Heisenberg–Landau Hamiltonian to our DFT calculated $|M|$–energy points, as shown in Figs. B1(a)–B1(c). We find that the fourth- and sixth-order expansions fail to accurately reproduce the energy profile, particularly for Mn_3RhSi and Mn_3IrSi. Incorporating eighth-order terms markedly improves the fitting quality and provides a more reliable description of the longitudinal spin fluctuations. Moreover, the fitted curves from the eighth-order expansion reproduce the $E_{DFT} - E_R$ profiles with excellent accuracy, confirming that the extracted Landau coefficients are convergent and unique. Therefore, the Landau expansion is truncated at the eighth order.

The Landau coefficients are extracted from DFT calculations with constrained magnetic moments,[30–33] where both the magnitude and direction of the local moments are fixed. The magnetic moment ($|M|$) — energy curve are obtained for the ground-state magnetic configuration by varying the local magnetic moment from approximately -1.0 μ_B to 1.0 μ_B using 20 constrained configurations. The quantity $E_{DFT} - E_R$, obtained by subtracting the Heisenberg exchange energy E_R from the DFT total energy E_{DFT}, can be expressed as the sum of the non-magnetic energy E_0 and the Landau expansion term E_L as a function of the $|M|$ (see Eq. (3)). By fitting the calculated $E_{DFT} - E_R$ curve, the Landau expansion coefficients A, B, C, and D are determined.

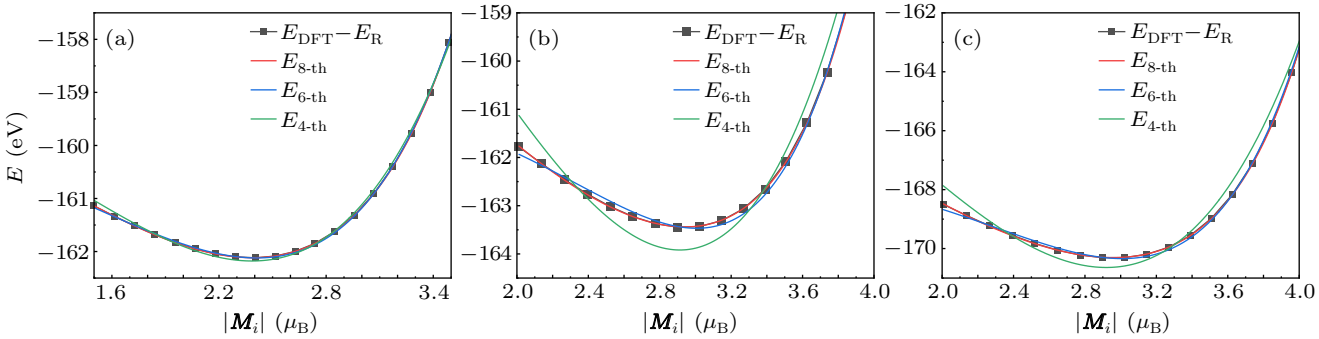


Fig. B1. Energy as a function of magnetic moment magnitude for (a) Mn_3CoSi, (b) Mn_3RhSi, and (c) Mn_3IrSi. $E_{\rm DFT}$ and $E_{\rm R}$ denote the DFT total energy and the Heisenberg exchange interaction energy, respectively. The black curve ($E_{\rm DFT}-E_{\rm R}$) shows the calculated spin-fluctuation energy associated with the magnetic moment magnitude ($|\boldsymbol{M}_i|$). The green, blue, and red curves ($E_{\rm 4\text{-}th}$, $E_{\rm 6\text{-}th}$, and $E_{\rm 8\text{-}th}$) correspond to the fitted energy curves using the fourth-, sixth-, and eighth-order expansions, respectively.

Acknowledgements

This work was supported by the National Key R&D Program of China (Grant No. 2023YFB4603801), National Natural Science Foundation of China (Grant No. 12474249), Guangdong Provincial Key Laboratory of Magnetoelectric Physics and Devices (Grant No. 2022B1212010008), the Major Key Project of Peng Cheng Laboratory (PCL), and the Fundamental Research Funds for the Central Universities (Grant No. 21625337).

References

[1] Wang R, Wang C, Li R, Guo D, Dai J, Zong C, Zhang W and Ji W 2025 *Chin. Phys. B* **34** 046801
[2] Xu L and Yang F 2024 *Chin. Phys. B* **33** 027101
[3] Li M, Ma H, Lou R and Wang S 2025 *Chin. Phys. B* **34** 017101
[4] Talanov M, Talanov V and Shirokov V 2017 *Russian Chemical Bulletin* **66** 1719
[5] Hopkinson J M, Isakov S V, Kee H Y and Kim Y B 2007 *Phys. Rev. Lett.* **99** 037201
[6] Jin H K and Zhou Y 2020 *Phys. Rev. B* **101** 054408
[7] Nakamura H, Yoshimoto K, Shiga M, Nishi M and Kakurai K 1997 *J. Phys.: Condens. Matter* **9** 4701
[8] Stewart J R, Rainford B D, Eccleston R S and Cywinski R 2002 *Phys. Rev. Lett.* **89** 186403
[9] Yamauchi H, Sari D P, Watanabe I, Yasui Y, Chang L J, Kondo K, Ito T U, Ishikado M, Hagihara M, Frontzek M D et al. 2020 *Communications Materials* **1** 43
[10] Yamauchi H, Sari D P, Yasui Y, Sakakura T, Kimura H, Nakao A, Ohhara T, Honda T, Kodama K, Igawa N, Ikeda K, Iida K, Ueta D, Yokoo T, Frontzek M D, Chi S, Fernandez-Baca J A, Kojima K M, Arseneau D, Morris G, Hitti B, Cai Y, Berlie A, Watanabe I, Hsu P T, Chen Y S, Lee M K, Hall A E, Balakrishnan G, Chang L J and Shamoto S i 2024 *Phys. Rev. Res.* **6** 013144
[11] Hall A E, Manuel P, Khalyavin D D, Orlandi F, Mayoh D A, Chang L J, Chen Y S, Jonas D G C, Lees M R and Balakrishnan G 2023 *Phys. Rev. Mater.* **7** 114402
[12] Shamoto S i, Yamauchi H, Iida K, Ikeuchi K, Hall A E, Chen Y S, Lee M K, Balakrishnan G and Chang L J 2023 *Commun. Phys.* **6** 248
[13] Ōnuki Y, Kaneko Y, Aoki D, Nakamura A, Matsuda T D, Nakashima M, Haga Y and Takeuchi T 2022 *J. Phys. Soc. Jpn.* **91** 065002
[14] Shamoto S, Yamauchi H, Hsu P T, Chang L J, Hall A E, Geetha B, Sakakura T and Kimura H 2022 *Experimental Reports* **28**
[15] Eriksson T, Lizárraga R, Felton S, Bergqvist L, Andersson Y, Nordblad P and Eriksson O 2004 *Phys. Rev. B* **69** 054422
[16] Kodama K, Honda T, Yamauchi H, Shamoto S i, Ikeda K and Otomo T 2021 *J. Phys. Soc. Jpn.* **90** 074710
[17] Hu M, Janson O, Felser C, McClarty P, Brink J V D and Vergniory M G 2025 *Nat. Commun.* **16** 8529
[18] Shamoto S i, Yamauchi H, Iida K, Ikeuchi K, Kaneko K, Chen Y S, Yano S i, Hsu P T, Lee M K, Hall A E, Balakrishnan G and Chang L J 2024 *Phys. Rev. Res.* **6** 033303
[19] Kresse G and Hafner J 1993 *Phys. Rev. B* **47** 558
[20] Kresse G and Furthmüller J 1996 *Phys. Rev. B* **54** 11169
[21] Blöchl P E 1994 *Phys. Rev. B* **50** 17953
[22] Perdew J P, Burke K and Ernzerhof M 1996 *Phys. Rev. Lett.* **77** 3865
[23] Momma K and Izumi F 2011 *Applied Crystallography* **44** 1272
[24] Ganose A M, Searle A, Jain A and Griffin S M 2021 *Journal of Open Source Software* **6** 3089
[25] Wang V, Xu N, Liu J C, Tang G and Geng W T 2021 *Computer Physics Communications* **267** 108033
[26] Zhang Y F, Ni X S, Chen K and Cao K 2025 *Phys. Rev. B* **111** 174451
[27] Yu H S, Ni X S, Yao D X and Cao K 2025 *Phys. Rev. B* **111** 094440
[28] Ni X S, Ji Y, He L, Xie T, Yao D X, Wang M and Cao K 2025 *npj Quantum Materials* **10** 17
[29] Ni X S, Yao D X and Cao K 2025 *J. Magn.d Magn. Mater.* **613** 172661
[30] Ma P W and Dudarev S L 2012 *Phys. Rev. B* **86** 054416
[31] Ruban A V, Khmelevskyi S, Mohn P and Johansson B 2007 *Phys. Rev. B* **75** 054402
[32] Rosengaard N M and Johansson B 1997 *Phys. Rev. B* **55** 14975
[33] Uhl M and Kübler J 1996 *Phys. Rev. Lett.* **77** 334
[34] Zhang Y F, Ni X S, Datta T, Wang M, Yao D X and Cao K 2022 *Phys. Rev. B* **106** 184422
[35] Hu X, Yao D X and Cao K 2022 *Phys. Rev. B* **106** 224423
[36] Liu Z, Ni X S, Li L, Sun H, Liang F, Frandsen B A, Christianson A D, dela Cruz C, Xu Z, Yao D X, Lynn J W, Birgeneau R J, Cao K and Wang M 2022 *Phys. Rev. B* **105** 214303
[37] Toth S and Lake B 2015 *J. Phys.: Condens. Matter* **27** 166002
[38] Eriksson T, Bergqvist L, Nordblad P, Eriksson O and Andersson Y 2004 *Journal of Solid State Chemistry* **177** 4058
[39] Eriksson T, Bergqvist L, Andersson Y, Nordblad P and Eriksson O 2005 *Phys. Rev. B* **72** 144427
[40] Stewart J R, Hillier A D, Hillier J M and Cywinski R 2010 *Phys. Rev. B* **82** 144439
[41] Yoshida H K 2022 *J. Phys. Soc. Jpn.* **91** 101003
[42] Paddison J A M, Stewart J R, Manuel P, Courtois P, McIntyre G J, Rainford B D and Goodwin A L 2013 *Phys. Rev. Lett.* **110** 267207
[43] Cao K, Lambert H, Radaelli P G and Giustino F 2018 *Phys. Rev. B* **97** 024420
[44] Robredo I, Schröter N B, Felser C, Cano J, Bradlyn B and Vergniory M G 2024 *Europhys. Lett.* **147** 46001